Identifying Metal–Halogen Bonding for Hydrogen-Induced Acid Generation in Bifunctional Catalysis

Yong Zhou, Martine Trentesaux, Maya Marinova, Sergei Chernyak, Jean-Charles Morin, Melanie Dubois, Samuel Eyley, Wim Thielemans, Vlad Martin-Diaconescu, Andrei Khodakov, et al.

ACS Catalysis

pubs.acs.org/acscatalysis Research Article

Identifying Metal−Halogen Bonding for Hydrogen-Induced Acid Generation in Bifunctional Catalysis

Yong Zhou, Martine Trentesaux, Maya Marinova, Sergei Chernyak, Jean-Charles Morin, Melanie Dubois, Samuel Eyley, Wim Thielemans, Vlad Martin-Diaconescu, Andrei Khodakov,* Jérémie Zaffran,* and Vitaly Ordomsky*

Cite This: ACS Catal. 2023, 13, 6351−6364 Read Online

ACCESS | Metrics & More | Article Recommendations | Supporting Information

ABSTRACT: Within conventional bifunctional catalysts, active metal sites are associated with metal components, while acid sites are usually localized over oxide supports. The modification of metal sites by halogens provides an opportunity to generate acidity via the heterolytic dissociation of hydrogen directly over metal sites. Herein, we report the results of high-throughput screening of the combinations of different metals (Co, Ni, Ru, Pt, Pd, Rh) and halogens (Cl, Br, I) for acid site generation from hydrogen in the hydrogenation of furfural and 5-hydroxymethylfurfural. The results demonstrate that only Pd and Pt catalysts demonstrate the formation of acid sites by interaction with Br, Cl, and I. The characterization in combination with density functional theory (DFT) modeling indicates hydrogen heterolytic dissociation over halogens localized at the edges and corners of Pd and Pt nanoparticles with an increase in strength of the acid sites with an increase of electronegativity of the halogen.

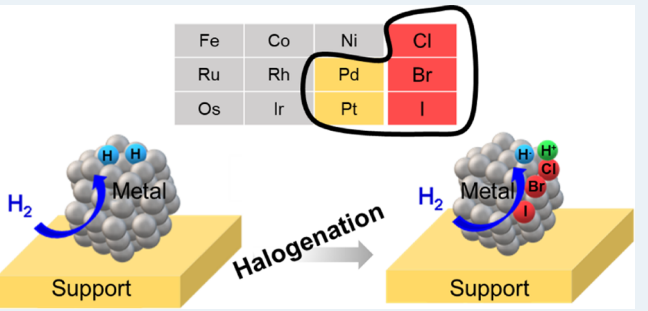

KEYWORDS: *metal, halogen, acidity, hydrogen, bifunctional catalysis, furfural, 5-hydroxymethylfurfural*

1. INTRODUCTION

Bifunctional heterogeneous catalysts integrate two types of active sites to combine different reactions in the same reactor and are widely used in numerous industrial processes for producing fuels and fine chemicals.[1−3] Among the bifunctional catalysts, metal−acid catalysts represent the most popular group of materials due to their application in hydrocracking, isomerization, hydrodeoxygenation, etc.[4−7] Traditionally, metal−acid bifunctional catalysts are constructed by deposition of a metal on an acidic support, for example, Pt/HY zeolite.[8] The influence of the key properties of metal−acid catalysts on their catalytic performance, such as the ratio of metal to acid sites, and their intimacy have been addressed extensively.[9−11] To maximize the catalytic benefits of bifunctional catalysts, it would be highly desirable to design an "ideal" bifunctional catalyst with sites combining both metal and acid properties to improve the synergistic effects between metal and acid sites in catalytic reactions.

Recently, modification of the metal catalyst with nonmetallic elements has become an efficient strategy to design highly selective bifunctional catalysts,[12,13] where the nonmetallic promoters exert both steric and electronic functionalities.[14,15] In addition, depending on the synthesis methods, the intimacy of metal and nonmetallic promoters can be tuned, which influences the catalytic behavior.[16,17] Among the nonmetal-promoted bifunctional catalysts, amine-, phosphine-, and sulfur-based catalytic systems have been successfully used in the selective hydrogenation of the aldehyde group, hydroperoxide production, etc.[18−20] In previous studies, we have observed that modification of Pd catalysts by iodine and bromine resulted in bifunctional catalysis during the hydrogenation of furfural and 5-hydroxymethylfurfural (HMF) toward ether and dimethylfuran, respectively. The generation of acidity has been proposed by the heterolytic dissociation of hydrogen over the halogen-metal sites.[21,22] Later, iodine-modified Pd nanoparticles were used for hydrogenative ring-opening reactions of C6 furan aldehydes to 2,5-hexanedione.[23] Hydrogenolysis of diphenyl ether has been studied over the Cl-modified Pt/γ-Al_2O_3 catalyst.[24]

It would be highly desirable to identify metal−halogen bonding providing acidity in the presence of hydrogen for further applications in catalysis. Here, we report the preparation and high-throughput catalytic screening of a variety of halogen-metal catalysts (supported Co, Ni, Ru, Rh,

Received: February 22, 2023
Revised: March 22, 2023
Published: April 24, 2023

https://doi.org/10.1021/acscatal.3c00845
ACS Catal. 2023, 13, 6351−6364

Pd, and Pt modified by Cl, Br, and I) (Figure 1). Biomass valorization reactions were chosen as probe reactions.

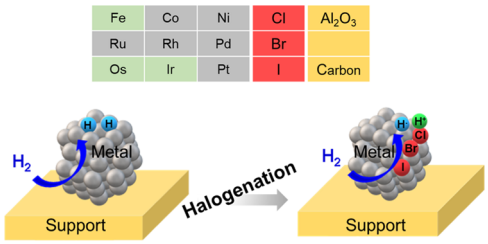

Figure 1. Scheme showing acid site generation on the halogenated metal catalyst.

Halogen-modified Pt and Pd catalysts were recognized as more efficient catalysts for etherification and deoxygenation reactions. Different characterization techniques combined with density functional theory (DFT) modeling were applied to reveal the relationship between the structure and catalytic performances of the materials.

2. EXPERIMENTAL SECTION

2.1. Materials. Catalysts Ru/Al_2O_3, Pd/Al_2O_3, Rh/Al_2O_3, Pt/Al_2O_3, Ru/C, Pd/C, and Pt/C with 5 wt % metal loadings, chlorobenzene (99.5%), bromobenzene (99%), iodobenzene (98%), furfural (99%), 5-(hydroxymethyl)furfural (HMF, 99%), 2-propanol (99.7%), tetrahydrofuran (THF, 99.9%), nickel nitrate hexahydrate ($Ni(NO_3)_2{\cdot}6H_2O$, 99.9%), and cobalt nitrate hexahydrate ($Co(NO_3)_2{\cdot}6H_2O$, 99.9%) were purchased from Sigma-Aldrich.

2.2. Catalyst Preparation. Ni/Al_2O_3 and Co/Al_2O_3 having 5 wt % metal loading were obtained by impregnation using Co and Ni nitrates ($Ni(NO_3)_2{\cdot}6H_2O$ and $Co(NO_3)_2{\cdot}6H_2O$) with subsequent drying and calcination at 500 °C. The catalysts were reduced at 400 °C for 3 h under a hydrogen flow.

In order to obtain the halogen-modified catalysts, 200 mg of supported metal catalysts was treated with a solution of 50 μL of chlorobenzene (ClPh), bromobenzene (BrPh), or iodobenzene (IPh) and 3 mL of isopropanol at 60 °C in 20 bar hydrogen for 1 h. The product was filtered and thoroughly washed in isopropanol. The catalysts were denoted as X-Pd/Al_2O_3, where X indicates halogen.

2.3. Catalyst Characterization. Scanning transmission electron microscopy (STEM) was performed on a TITAN Themis 300 S/TEM microscope equipped with a probe aberration corrector and a monochromator, allowing spatial resolution of 70 pm and energy resolution of 150 meV, a super-X windowless 4 quadrant SDD (silicon drift detector) detection system for STEM-EDX mapping, and several annular dark field detectors. Measurements were performed with a spot size of about 500 pm, a semiconvergence angle between 20 mrad, and a probe current of approximately 100 pA. The collection angles were selected between 50 and 200 mrad for HAADF images.

X-ray photoelectron spectra were acquired on a Kratos Axis Supra photoelectron spectrometer using a monochromatic Al Ka X-ray source (1486.7 eV, 120 W) with hybrid (magnetic/electrostatic) optics. All of the spectra were acquired at normal emission with the analyzer in the fixed analyzer transmission mode. Survey spectra were acquired with a pass energy of 160 eV and high-resolution spectra with a pass energy of 20 eV. All of the spectra were acquired under charge neutralization conditions, with the samples isolated from the instrument ground to prevent differential charging and charge neutralization provided using a low-energy electron gun within the field of the magnetic lens. Spectra were analyzed using CasaXPS version 2.3.25PR1.0. Spectra were charged referenced to C at 284.5 eV. Elemental quantification was performed using empirical relative sensitivity factors supplied by Kratos Analytical, and the resulting elemental concentrations represent the homogeneous equivalent composition of the samples. No correction for sample morphology or in-depth distribution of elements was performed.

X-ray absorption spectra (XAS) of powder pellets were acquired at the Pd K-edge, Pt L3-edge, and Br K-edge on samples diluted in cellulose when necessary. XAS spectra were collected in the transmission mode at room temperature employing an Si311 double-crystal monochromator available at the CLAESS beamline of the ALBA synchrotron. Several XAS repeats were collected to ensure reproducibility and statistics. Spectra processing and analysis were carried out with the Athena software package.[25] The energy scale was calibrated by setting the first inflection point of the Pd metal foil to 24,350.0 eV for Pd K-edge data and the Pt metal foil to 11,564.0 eV for Pt L3-edge data. EXAFS were extracted using the background subtraction by AUTOBK algorithm employing R_{bkg} of 1.0 (Pd K-edge) or 1.2 (Pt L3-edge) in the 0−15.9 $Å^{-1}$ region of k-space. Principle component analysis was carried out prior to linear combination fitting, and it was found that halobenzene-treated carbon-supported metal catalysts require up to three components to be fully described: the corresponding metal foil, carbon-supported metal catalyst, and metal halide ($PtCl_2$, $PtBr_2$, PtI_2, $PdCl_2$, $PdBr_2$, PdI_2).

The infrared spectra for CO adsorption were recorded on a Thermo Scientific Is 50 equipped with a KBr beam splitter and a mercury cadmium telluride (MCT) detector. All IR spectra were recorded with 2 cm^{-1} resolution and 64 scans and were normalized to a disc of 5 mg cm^{-2}. Samples were pretreated under H_2 (100 mbar) at 60 °C overnight and then evacuated under high vacuum for 3 h. CO was then added at room temperature in doses until saturation. The acidity was measured via pyridine (Py) adsorption, and the measurements were performed via activation at 150 °C under vacuum at 10^{-6} Torr overnight. Pyridine adsorption was carried out at 1.2 mbar with and without a hydrogen atmosphere.

2.4. Computational Details. This work was performed in the framework of periodic density functional theory (DFT), with VASP software.[26,27] We chose the Perdew−Burke−Ernzerhof (PBE) exchange−correlation (XC) functional[28] since GGAs (generalized gradient approximations) are known for their efficiency in metal calculations. We fixed the energy cutoff to 400 eV to model the ion−electron interaction in the projected augmented wave (PAW) formalism.[29] For the k-mesh, we used 3 × 3 × 1 k-points according to the Monkhorst−Pack scheme.[30] The electronic and the ionic convergence criteria were set to 10^{-6} eV and 0.05 eV/Å, respectively. All of these parameters allow obtaining an accuracy of ∼0.05 eV for adsorption and reaction energy computation. The following results are presented without zero-point-energy (ZPE) and entropy correction at zero K temperature.

We focused here on Pt and Pd, presenting an fcc geometry. After optimizing the bulk, we cleaved it along the (111) plane and prepared flat and stepped surfaces for the two metals. We

https://doi.org/10.1021/acscatal.3c00845
ACS Catal. 2023, 13, 6351−6364

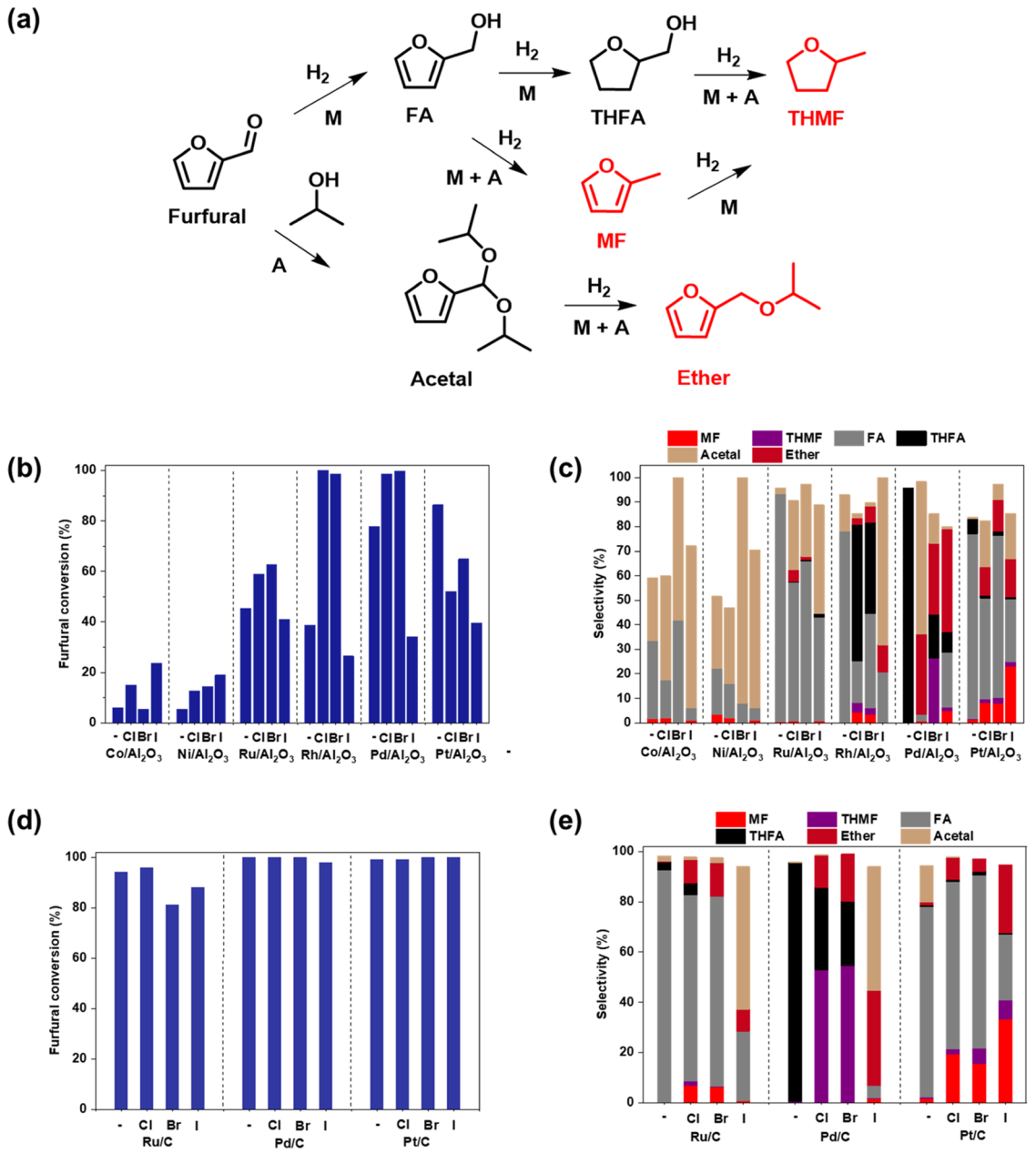

Figure 2. Scheme of the reaction (a) and furfural conversion and product selectivity during furfural hydrogenation over alumina (b, c) and carbon (d, e) metal catalysts with and without halogen modification. Reaction conditions: 2.4 g of isopropyl alcohol, 0.1 g of furfural, and 30 mg of catalyst, 20 bar H_2, 60 °C, 1 h.

built a (3×3) and a (10×3) slab for the flat and the stepped models, respectively, both of them with a four-atom-layer thickness. The two bottom layers were frozen in a bulk-like structure. Also, we fixed a vacuum of 15 Å in the z direction, and we ensured such dimensions prevent any lateral and vertical interactions between the virtually replicated images.

2.5. Catalyst Evaluation. The furfural hydrogenation reaction was performed in SPR high-throughput equipment, which has 24 parallel reactors. In each vial, 2.4 g of 2-propanol, 0.1 g of furfural, and 30 mg of catalyst were added. Afterward, all of the vials were flashed and pressurized with 20 bar of hydrogen at room temperature. Then, the vials were heated to 60 °C with continuous shaking for 1 h. Afterward, the vials were cooled down and the reaction solutions were separated by filtration and analyzed by GC.

The HMF hydrogenation reaction was performed in a 25 mL stainless-steel autoclave equipped with a magnetic stirrer. 0.1 g of HMF, 5 g of THF, and 50 mg of catalyst were added into the reactor. Afterward, the reactor was flashed and pressurized with 20 bar of hydrogen at room temperature. Then, the autoclave was heated to 60 °C with continuous magnetic stirring for 3 h. When the reaction finished and the autoclave was cooled down, the reaction solutions were separated by filtration and analyzed by GC. The conversion of furfural and HMF and selectivity to corresponding products can be defined as follows

$$\text{conversion}\ (\%) = 1 - \frac{n_A}{n_A^0}$$

https://doi.org/10.1021/acscatal.3c00845
ACS Catal. 2023, 13, 6351−6364

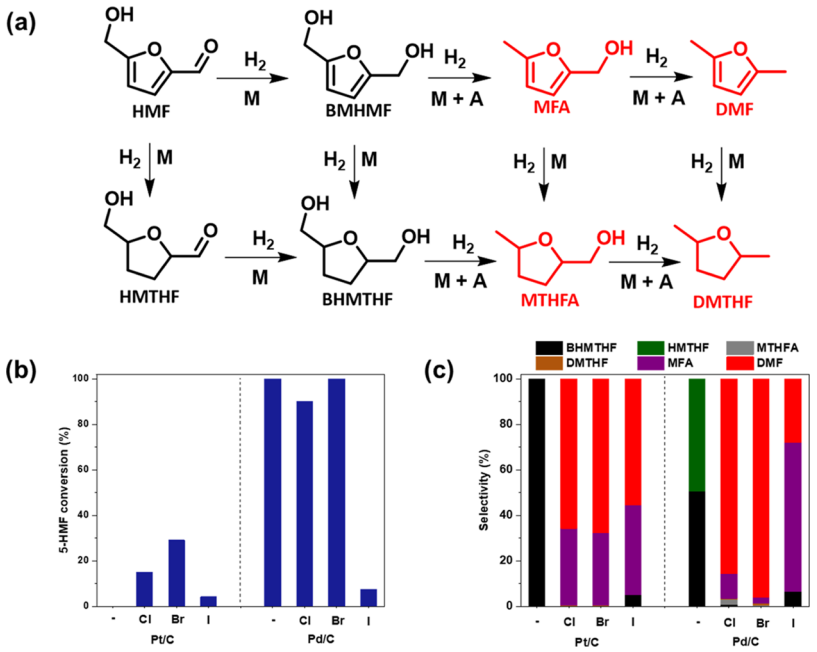

Figure 3. Scheme of the reaction (a) and 5-HMF conversion (b) and product selectivity (c) during furfural hydrogenation over Pt/C and Pd/C catalysts with and without halogen modification. Reaction conditions: 5.0 g of THF as a solvent, 0.1 g of 5-HMF, and 50 mg of catalyst, 20 bar H_2, 60 °C, 3 h.

$$\text{selectivity to the product } p\ (\%) = \frac{n_p}{n_A^0 - n_A}$$

where n_A, n_A^0, and n_p refer to the final and initial moles of furfural and HMF and the number of moles of product. The carbon balance was higher than 90% for HMF hydrogenation using anisole as a standard.

The esterification of acetic acid with ethanol was performed by mixing in an autoclave of 30 mg of catalyst, 20 mmol of ethanol, and 20 mmol of acetic acid with magnetic stirring under 20 bar H_2 or N_2 at 80 °C for 3 h.

3. RESULTS AND DISCUSSION

3.1. Catalytic Evaluation of the Metal−Halogen Catalysts. *3.1.1. High-Throughput Screening Metal−Halogen Catalysts for Furfural Hydrogenation.* The catalysts were prepared by treatment of commercial alumina and carbon-supported metal catalysts containing about 5 wt % metal by PhCl, PhBr, and PhI at 60 °C under a hydrogen atmosphere. The elemental analysis data are given in Table S1, SI. The catalysts were tested in the hydrogenation of furfural. As depicted in Figure 2, in the presence of isopropyl alcohol as a solvent, the reductive transformation of furfural yields multiple products (Figure S1, SI). There are generally three types of reactions: (1) conversion of furfural to furfuryl alcohol (FA) and tetrahydrofurfuryl alcohol (THFA) by hydrogenation over metal sites,[31] (2) reaction of furfural with isopropanol to form an ether through an intermediate acetal over medium-strength acid sites,[32] and (3) deoxygenation of furfuryl alcohol to methylfuran (MF) and methyl tetrahydrofuran (THMF), which requires strong acid sites.[33]

All of the metal catalysts were tested in the furfural hydrogenation reaction in a high-throughput reactor. As shown in Figure 2, the furfural conversion is negligible (∼ 6%) over Co/Al_2O_3 and Ni/Al_2O_3 catalysts. Noble metal catalysts (Ru, Rh, Pd, and Pt) without halide pretreatment show furfural conversions in the range of 39−86%, which is higher in comparison with transition metals. Halogenation of Co and Ni catalysts increases the catalytic activity; however, it is still very low.

The increase in catalytic activity was observed for Ru, Rh, and Pd metal catalysts in the presence of Cl and Br, but the activity decreased for I-treated catalysts. On the other hand, among the series of halogen-treated noble metal catalysts, the Pt-based catalysts showed lower activity than the parent material, regardless of the type of halogen.

FA and acetal were the main products over Co- and Ni-based catalysts for both initial and halogenated samples (Figure 2). The parent noble metal catalysts (Ru/Al_2O_3, Rh/Al_2O_3, and Pt/Al_2O_3) exhibit high selectivity to FA, demonstrating their high hydrogenation ability of the carbonyl group. However, Pd/Al_2O_3 shows a better hydrogenation performance with the hydrogenation of the aromatic ring of furfural to THFA.

Ru/Al_2O_3 shows an increase by 20−30% in the contribution of acetal in the products after halogenation of the catalyst, which could be explained by the generation of weak acid sites. At the same time, the Rh/Al_2O_3 catalyst treated by PhCl and PhBr shifted the selectivity from FA to THFA, while acetal was mostly produced over the PhI-treated catalyst. The products related to metal−acid bifunctional catalysts like MF, THMF, and ether were undetectable. However, these products were observed after the halogenation of Pd/Al_2O_3 and Pt/Al_2O_3 catalysts. The selectivity to THFA over halogenated Pd/Al_2O_3 was significantly reduced with the generation of ether with a selectivity of 30−40% as one of the main products. In addition, acetal, THMF, and FA were observed after modification by Cl, Br, and I, respectively. Pt/Al_2O_3 after pretreatment still produced FA as the main product, however, with a selectivity of 10% for ether and an increase in the selectivity to MF in the order Cl < Br < I reaching 20%. Thus, these results

https://doi.org/10.1021/acscatal.3c00845
ACS Catal. 2023, 13, 6351−6364

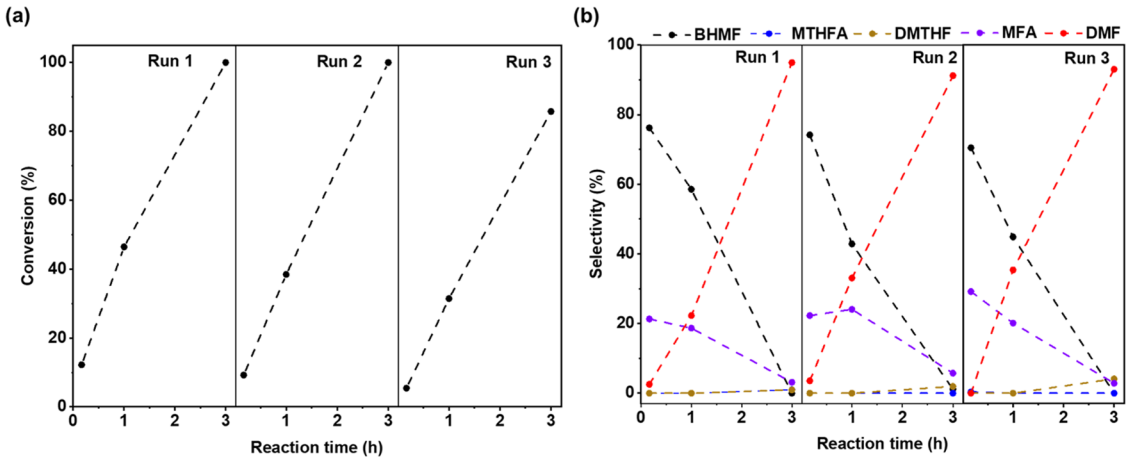

Figure 4. Conversion (a) and selectivity (b) for the first three cycles with reaction time. Reaction conditions: 5.0 g of THF as a solvent, 0.1 g of 5-HMF, and 50 mg of Br-Pd/C catalyst, 20 bar H_2, 60 °C.

demonstrate the presence of acid sites after treatment by halogens of Pt and Pd catalysts.

The support usually plays an important role in the activity of catalysts due to the different sizes of metal nanoparticles and their interaction with the support.[34,35] Pt and Pd have been selected as metals generating acidity with Ru as a reference for the preparation of carbon-supported catalysts.

Carbon-supported catalysts showed high furfural conversion, reaching almost full conversion of furfural. The modification of Pd/C by Cl and Br resulted in a significant increase in the selectivity toward THMF to 50% with the lower contribution of ether as a product in comparison with I-Pd/C, demonstrating still high selectivity to ether. It indicates an increase in the strength of the acid sites with an increase in the electronegative character of halogen I < Br ≈ Cl. This result agrees completely with our earlier results[21,22] for etherification of furfural and hydrogenolysis of HMF to DMF over the Pd catalyst treated by I and Br, respectively. The Pt/C catalyst before and after treatment by halogens demonstrated a performance similar to that of Pt/Al_2O_3 with an increase in contribution of MF and ether.

3.1.2. Metal–Halogen Catalyst for 5-HMF Hydrodeoxygenation Conversion. In order to demonstrate the general patterns of this performance, the Pt/C and Pd/C promoted and nonpromoted by halogens were tested in the hydrogenation of 5-hydroxymethylfurfural (Figures 3 and S2, SI). Pd/C demonstrated a much higher activity than Pt/C with the formation of 2,5-bis(hydroxymethyl)tetrahydrofuran (BHMTHF) and hydroxymethyltetrahydrofurfural (HMTHF) as the main products of HMF hydrogenation. Treatment with Cl and Br changes the route of hydrogenation to dimethylfuran (DMF) as the product of HMF deoxygenation, reaching a selectivity higher than 90%. In correlation with furfural hydrogenation, treatment by iodine suppressed activity with less-pronounced deoxygenation to methylfurfuryl alcohol (MFA). At the same time, Cl and Br promoted Pt/C catalysts for the deoxygenation of HMF to the mixture of DMF and MFA. Treatment by iodine did not show reasonable activity in furfural hydrogenation. The comparison of the catalytic performance of all of these catalysts at the conversion of about 30% by variation of reaction time (Table S2, SI) demonstrates a higher selectivity to DMF for halogen-treated Pt/C catalysts in comparison with Pd/C, producing more BMHMF and MFA as intermediate products.

The possible explanation of bifunctional catalysis after the modification of metal catalysts by halides is the generation of hydrogen halides resulting in homogeneous acidic catalysis. In order to verify the stability of the bifunctional catalyst, the hydrogenation of HMF was performed over the Br-Pd/C catalyst as the most selective to DMF by three consecutive cycles with intermediate separation by centrifugation and washing in THF (Figure 4). The catalyst shows comparable catalytic activity with a slight decrease in activity due to the loss of the catalyst during sampling. The catalyst demonstrates intermediate hydrogenation of HMF to BHMF with MFA and finally to DMF, with similar behavior for all three cycles. The additional catalytic tests of Br and Cl-Pd/C for 5 cycles with analysis only after 3 h of the test show no visible deactivation at high selectivity to DMF (Figure S3, SI). These results indicate the heterogeneous nature of halogenated bifunctional catalysts.

Metallic catalysts usually require high temperatures (>150 °C) for DMF and MF syntheses from HMF and furfural, respectively, and in the presence of acid catalysts, the temperature is significantly lower.[36−38] The metal−acid bifunctional catalysts provide hydrogenation of carbonyl groups, with acid sites responsible for C−OH bond protonation and hydrogenolysis over metal sites to the methyl group. It requires high intimacy of metal and acid sites, which is hard to achieve using conventional heterogeneous catalysts. This is why the most efficient bifunctional catalysts at the moment are based on the combination of heterogeneous metallic and homogeneous acidic catalysts.[39]

The generation of acidity over halogenated metal catalysts could also be used for purely acidic catalysis (Figure S4, SI). For example, the esterification of ethanol and acetic acid over the Br-Pd/C catalyst in inert gas shows a conversion similar to the blank test or over Pd/C. However, the activity of Br-Pd/C increased after the introduction of hydrogen, indicating the generation of acid sites for the esterification reaction as well. It means that the catalyst can be used not just for bifunctional catalysis.

Our results indicate a major increase in both reactivities over Pd and Pt catalysts promoted by Cl and Br toward the products of bifunctional metal−acid catalysis. These catalysts combine metal and acid sites for highly efficient deoxygenation of furfural to MF and THMF and HMF to DMF and MFA. Treatment by iodine generally suppresses activity and results in

https://doi.org/10.1021/acscatal.3c00845
ACS Catal. 2023, 13, 6351−6364

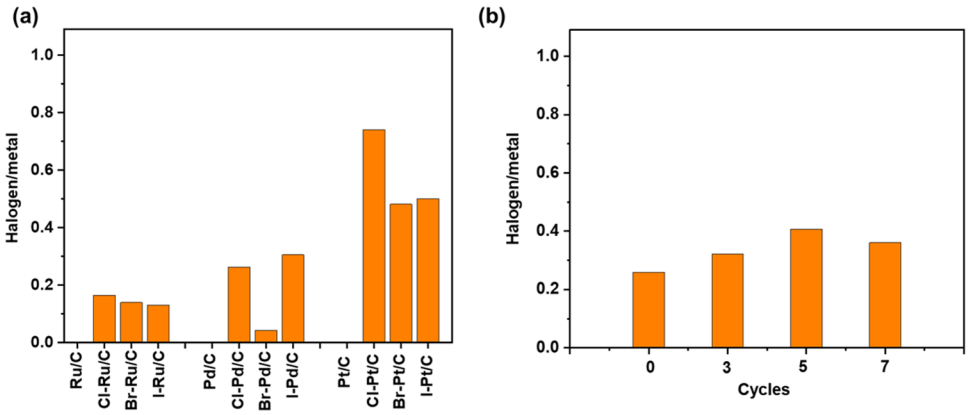

Figure 5. Ratio of halogens to metals for Pt, Pd, and Ru supported over carbon (a) and the ratio in the Cl-Pd/C catalyst after catalytic cycles of hydrogenation of HMF (b).

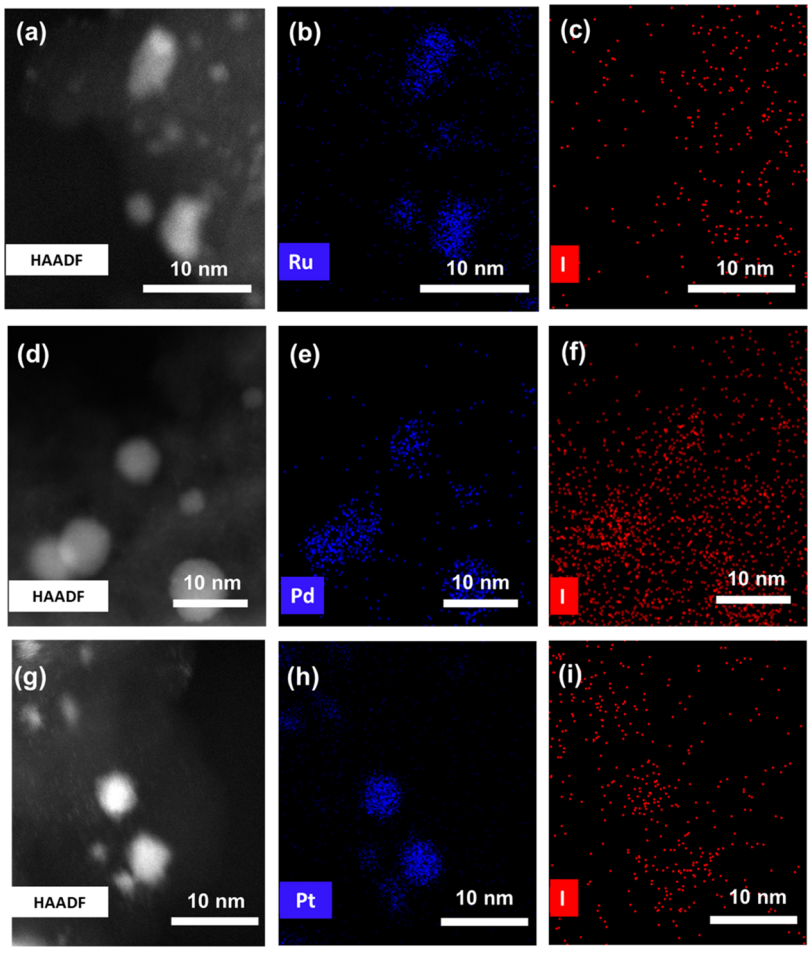

Figure 6. HAADF-STEM images and elemental mapping of metal−halogen catalysts. HAADF-STEM images of I-Ru/C (a), I-Pd/C (d), and I-Pt/C (g). Elemental mappings of Ru (b), Pd (e), Pt (h), and I (c, f, i) of I-Ru/C, I-Pd/C, and I-Pt/C.

the formation of products corresponding to milder acidity. In order to provide further insights into the enhancement of catalytic performances over metal−halogen catalysts, we used various characterization techniques and DFT modeling for Pt, Pd, and Ru catalysts.

3.2. Characterization of Catalysts. The analysis of the content of halogens over Pt/C, Pd/C, and Ru/C catalysts was performed using XPS. Figure 5 shows the ratio of halogen to metal in the catalysts before and after the reaction. The ratio of halogen to metal decreased in the order Pt ≫ Pd > Ru from 0.5 to 0.1. Interestingly, the lowest content is observed for the Br-treated Pd catalyst; however, the catalyst demonstrates high efficiency for deoxygenation of HMF to DMF. It means that even a small content of halogen is enough for modification of the catalytic performance as, for example, it has been observed earlier for a trace amount of Bi over Fe in Fischer−Tropsch synthesis.[40] Analysis of the other metal catalysts shows that Co and Ni have negligible quantities of halogens on the surface in

https://doi.org/10.1021/acscatal.3c00845
ACS Catal. 2023, 13, 6351−6364

comparison with noble metals (Table S3, SI), which could be due to the low conversion of the halogen precursor or weak interaction between halogen and transition metals. The ratio of halogen to metal measured for Cl-Pd/C does not show significant changes even after seven cycles, indicating the high stability of the catalyst at the reaction conditions (Figure 5).

The I-Ru/C, I-Pd/C, and I-Pt/C catalysts were subjected to STEM-EDS analysis to determine the localization of halogens in the catalysts (Figure 6). The HAADF images show the size distribution of metal nanoparticles (Figure S5, SI) for all three samples. The size of metal nanoparticles decreases in the order Pd (5.2 nm) ≫ Ru (1.8 nm) ≈ Pt (1.2 nm). Compared to alumina, the carbon support significantly improves the dispersion of metal nanoparticles due to the higher surface area and weak interaction with the metal. Thus, the size of Pt nanoparticles decreases from 5.6 for Al_2O_3 to 1.2 nm for the carbon support (Figure S6, SI). This could explain the stronger effect of halogen on the carbon-supported metal catalysts in comparison with alumina. The STEM-EDS analysis (Figure 6) indicates the spatial coexistence of both halogen and Pd and Pt metal elements and a potential modifying effect of halogens on metal nanoparticles. Analysis of the distribution of halogens over other catalysts also shows that halogens are always present on the surface of metal nanoparticles (Figure S7, SI).

FTIR spectroscopy of CO adsorption was used to further confirm the localization of halogens using alumina-supported catalysts due to the nontransparency of carbon to IR irradiation (Figure 7). A set of CO absorption bands was

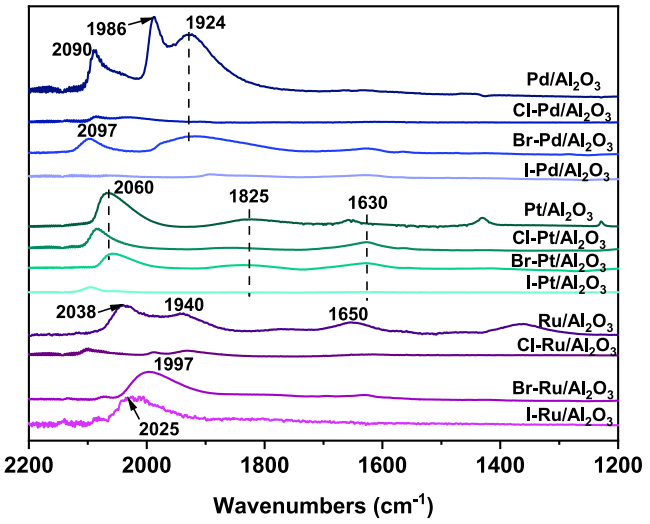

Figure 7. CO-FTIR of metal catalysts without and with modification by Cl, Br, and I halogens.

observed on the nonpromoted Ru/Al_2O_3, Pd/Al_2O_3, and Pt/Al_2O_3 catalysts. The main bands at 2090 cm^{-1} for Pd/Al_2O_3, 2060 cm^{-1} for Pt/Al_2O_3, and 2038 cm^{-1} for Ru/Al_2O_3 are due to CO linearly adsorbed on metallic Pd, Pt, and Ru nanoparticles with localization of CO at edges and corners of metal nanoparticles.[41−44] The low wavenumber bands at 1940 cm^{-1} for Ru/Al_2O_3, 1825 cm^{-1} for Pt/Al_2O_3, and 1986 and 1924 cm^{-1} for Pd(100) and (111) facets of Pd/Al_2O_3 are characteristic of bridge-bonded CO adsorption over the planes. The bands at lower wavenumbers are usually assigned to multiple-bonded CO adsorption.

The treatment by iodine resulted in significant suppression of CO adsorption on Pd/Al_2O_3 and Pt/Al_2O_3, which could be related to the strong electronic effect and hindrance effect of iodine on the metal. The high affinity of iodine for Pd and Pt sites explains the low catalytic activity of iodine-treated catalysts (Figures 2 and 3). It is interesting to note that I-Ru/Al_2O_3 had no bridged-bonded CO adsorption with a single peak at 2025 cm^{-1} of linearly adsorbed CO. This could be explained by the interaction of iodine mainly with planes of Ru nanoparticles avoiding interaction with edges and corners, which corresponds to an earlier study.[45]

Treatment of Ru/Al_2O_3 by bromine results in an effect similar to that by iodine with a red shift of the linearly adsorbed CO band to 1997 cm^{-1}, which could be related to electron transfer to the antibonding orbital of CO with a decrease in the C═O frequency. At the same time, treatment by Cl leads to the suppression of CO adsorption over both Ru and Pd catalysts, which could be assigned to the strong electron-withdrawal effect of Cl. The modification of Pd by Br leads to a significant decrease in the bands related to linear and bridge-bonded CO adsorption, indicating the interaction of Br mainly with the edges and corners of Pd atoms. The modification of Pt by Br and Cl shows a significant decrease in the intensity of linearly adsorbed CO, indicating the interaction mainly with edges and corners as well.

The generation of acidity over halogenated metal catalysts can be confirmed by analysis of Py adsorption in the presence of hydrogen.[22] Chemically adsorbed pyridine over the catalysts without the addition of hydrogen results in the usual set of bands at 1450, 1485, and 1605 cm^{-1} related to Py adsorption on Lewis acid sites of the Al_2O_3 support (Figure S8, SI). It has to be noted that there are no bands at about 1540 cm^{-1} related to Py adsorption over Brønsted acid sites. The addition of hydrogen shows the appearance of weak bands at 1540 and 1535 cm^{-1} over I-Pt/Al_2O_3 and I-Pd/Al_2O_3, which could be assigned to the generation of Brønsted acidity by hydrogen dissociation (Figure 8). It is interesting to note that in the presence of Br the amount of Brønsted acid sites significantly increased on the Pd catalyst. A similar effect was less pronounced for the Pt catalyst. Treatment by Cl shows a small number of acid sites over Pd and no visible acidity over the Pt catalyst. Ru catalysts modified by I, Br, and Cl showed no generation of acid sites following poor catalytic perform-

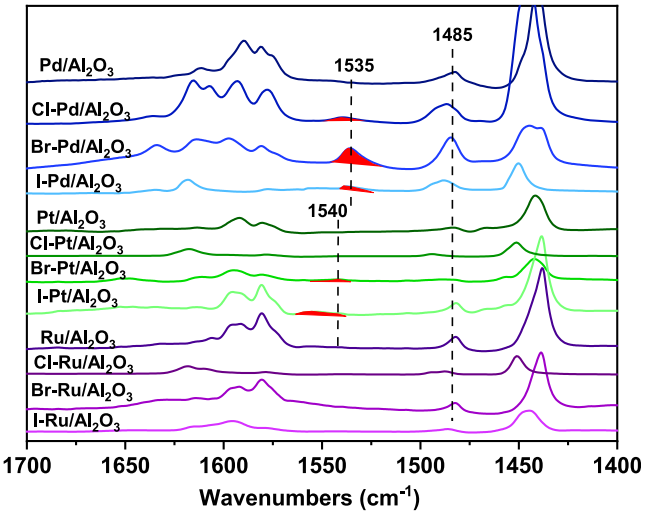

Figure 8. Py-FTIR of metal catalysts in the presence of hydrogen without and with modification by Cl, Br, and I halogens.

https://doi.org/10.1021/acscatal.3c00845
ACS Catal. 2023, 13, 6351−6364

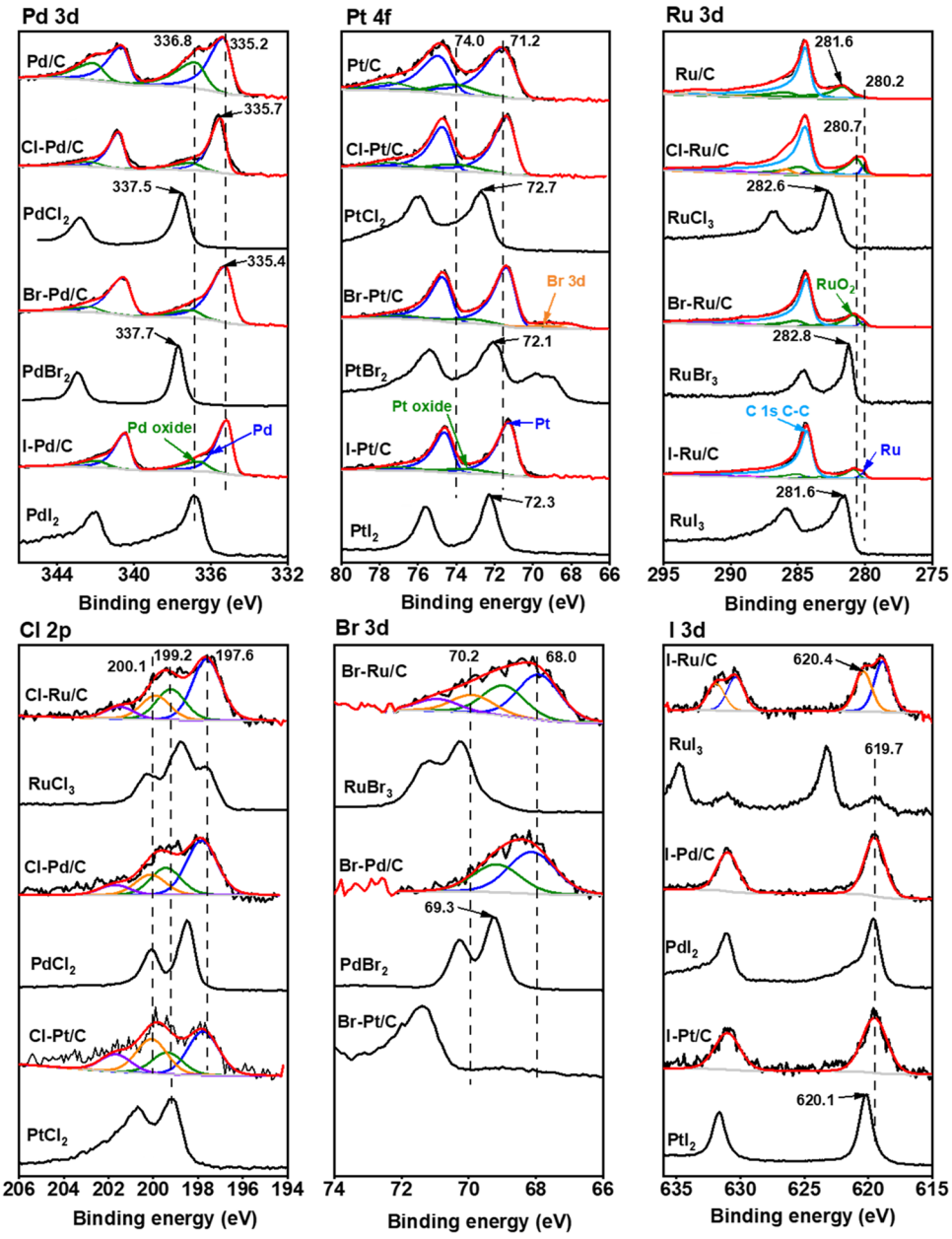

Figure 9. XPS spectra of Pd, Pt, and Ru/C catalysts and halogens for the parent and halogen-treated catalysts.

ance (Figures 2 and 3). Thus, the highest acidity is observed for the Br-Pd/C catalyst with a small content of Br and the highest efficiency for HMF deoxygenation to DMF. Bifunctional catalysis and especially halogenated metal catalysts require the optimum ratio of both metal and acid sites. Most probably, the presence of a high amount of Cl and I over the metal surface suppresses the hydrogenation and hydrogen dissociation ability, leading to low acidity and catalytic efficiency in comparison with other catalysts. In comparison with Pt and Pd, metals like Rh and Ru do not show the generation of acid sites, which according to FTIR could be assigned to the localization of halogens more over the planes for the latter.

The electronic states of metals and halogens in the carbon-supported catalysts were characterized by XPS. As shown in Figure 9, the Pd 3d spectra have two doublets with BE (Pd $3d_{5/2}$) at 335.3 and 336.8 eV assignable to metallic Pd^0 and Pd^{2+} (PdO), respectively. The deconvoluted spectrum of Pt/C also presents two doublets with BE at 71.2 and 74.0 eV corresponding to Pt and Pt^{4+} (PtO_2), respectively. The Ru/C spectrum is characterized mainly by the Ru $3d_{5/2}$ peak at 281.6 eV, indicating the presence of hydrated RuO_2 due to the high oxophilicity of Ru. It should be noted that the halogenation does not result in a statistically significant shift of the metal peak in comparison with the significant effect of halogenation on FTIR CO adsorption (Figure 7). However, for example, the peak assigned to the oxidized Pd species shifts to a lower BE from Cl-Pd/C to I-Pd/C in a way similar to the reference salts. The effect is especially noticeable for catalysts reduced prior to XPS analysis (Figure S9, SI) and could be explained by the presence of surface halide species. The reference metal salts demonstrate a more pronounced shift due to the withdrawal of electrons from metal. A decrease of BE from 337.5 eV for $PdCl_2$ to 336.8 eV for PdI_2 is observed, which is similar for Pt and Ru salts (Figure 9). In the row from Cl to I, the interaction between halogen and metal changes from an ionic to a more

https://doi.org/10.1021/acscatal.3c00845
ACS Catal. 2023, 13, 6351−6364

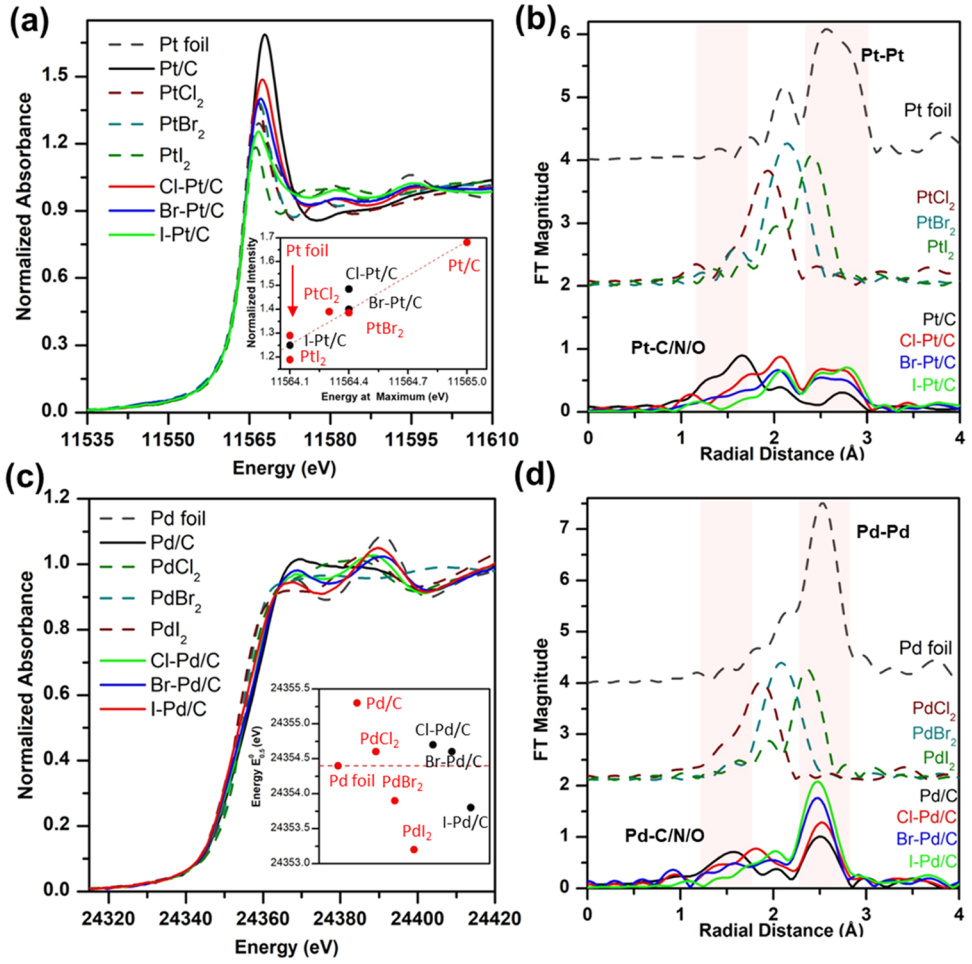

Figure 10. XANES and Fourier-transformed (FT) EXAFS for (a, b) Pt L3-edge for Pt catalysts and (c, d) Pd K-edge for Pd catalysts. FT was carried out using a Hannings window over a *k*-range of 3−13.9 $Å^{-1}$. Insets show markers of effective oxidation state, where for (a) normalized white line intensity vs white line maximum energy for Pt L3-edge data are plotted; and (c) rising edge energy at half height of the normalized spectra for Pd K-edge data are plotted.

covalent character, resulting in a higher electronic density over the metal.

The Cl 2p XPS shows a well-resolved doublet corresponding to Cl^- as an anion with peaks at $2p_{3/2}$ 198.5 eV for $PdCl_2$ and 199.2 eV for $PtCl_2$. $RuCl_3$ demonstrates, besides a doublet at 200.3 and 198.7 eV, an additional peak at a lower BE. According to the literature, this is the result of partial hydrolysis of $RuCl_3$ resulting in the appearance of HCl.[46] It is interesting to note that all Cl-treated metal catalysts contain doublets at the positions of $2p_{3/2}$ with a higher intensity at 197.6 and a lower one at 200.1 eV. The second peak is usually attributed to covalently bonded Cl and could be assigned to unconverted PhCl or Cl attached to the carbon support.[47] The amounts of organic halides in XPS spectra decrease from Cl to I, and they are always present in Ru/C catalysts most probably due to difficulties in the activation of the C−Hal bond over Ru nanoparticles. The first peak is in the region corresponding to the Cl^- ion;[48] however, it is significantly shifted to a lower BE in comparison with Pt, Pd, and Ru chlorides. This shift can be explained by the withdrawal of electrons to chlorine atoms supported over metal nanoparticles due to the reduced number of chlorine atoms per metal center when compared with the reference salt materials.

A similar effect has been observed in the Br 3d XPS spectra for Br-treated catalysts with a shift of the peaks by 1−2 eV to the same localization at a lower BE for Br-treated metal catalysts in comparison with salts. However, there is a similar localization of the peaks for iodine in the treated catalysts in comparison with salts due to the lower electronegativity of iodine. It should be noted that a significant part of iodine is oxidized, with the formation of iodine oxide shifted to a higher BE.[49]

XPS analysis after the reaction shows a similar state of metals and halogens, indicating high stability of the catalysts (Figure S10, SI).

To confirm the interaction of halogen with the metals, we have used X-ray adsorption spectroscopy (XAS) (Figure 10). Both Pd/C and Pt/C show rising edge features consistent with a more effectively oxidized metal center than the corresponding metal (0) foils. Furthermore, the EXAFS signals show features at 1.58 and 1.67 Å in the *r*-space for Pd/C and Pt/C, respectively, attributable to metal−O bonds and between 2.5 and 3.0 Å due to metal−metal interactions. This is consistent with XPS data showing the presence of metal oxides and low-valence metallic centers present in the carbon-supported metal catalysts. Upon treatment with halobenzenes, the XAS spectra show an effective reduction of the metal centers with rising edge energies and intensities following a similar trend observed in the metal-halide references, correlating with the electronegativities of Cl, Br, and I. This points to a direct effect on the

https://doi.org/10.1021/acscatal.3c00845
ACS Catal. 2023, 13, 6351−6364

metal center from the type of halide. Furthermore, although the EXAFS signal clearly shows the formation of metallic nanoparticles, the resulting XANES spectra differ from that of the metal (0) reference foils, which indicates a more complex picture, where multiple species are present. Linear combination analysis (Figure S11, Table S4, SI) of halobenzene-treated samples shows that in addition to increasing the metal nanoparticle formation, increasing metal-halide character is generally observed going from Cl to Br to I halobenzenes in the carbon-supported metal catalyst, again pointing to direct halo−metal interaction. A halo−metal interaction is also supported by scattering features at ∼2 Å in the r-space of the Fourier-transformed EXAFS signal for the series where scattering from metal−halogen bonds is dominant. Further support for a halo−metal interaction also comes from the Br K-edge (Figure S12, SI), where Pd/C- and Pt/C-treated samples showed similar rising profiles but shifted following the electronegativity trends for Pd and Pt as seen in the $PtBr_2$ and $PdBr_2$ references with Br-Pt/C at a higher energy relative to Br-Pd/C.

Thus, the characterization results show the presence of Cl, Br, and I over Pd and Pt metal nanoparticles with the generation of Brønsted acid sites in the presence of hydrogen. Ru does not demonstrate the generation of acid sites with localization of halogens over the planes of nanoparticles in comparison with edges and corners for Pt and Pd. The interaction has a more covalent character in the presence of I, suppressing both adsorptions of molecules and activity of the catalysts.

3.3. DFT Modeling. In order to provide a better understanding of the acidic sites generated by halide adsorption at metals, we performed a DFT study to address the surface acidity. We only focused on Pd and Pt in this part, considering they give the effect of acidity generation. In order to address defect and particle size effects, we used both flat and stepped (111) surface models. Since the process takes place in a highly reductive atmosphere, we assume the surface is almost completely covered with hydrogen. Hence, using the pyridine molecule as a probe, it is possible to correlate the reaction energy of its conversion into pyridinium ion to the Brønsted acidity of the surface (Figure 11). We investigated this property for metallic surfaces with preadsorbed halogens, PdX and PtX (X: Cl, Br, and I), and clean metal surfaces.

While the pyridine molecule is in the gas phase, we coadsorbed together a halide and a hydrogen atom to simulate the reagent state for both flat and stepped models. On the other hand, the product state was modeled by coadsorbing halide and pyridinium. After an extensive configurational study (see details in the SI, Figures S13−S16, SI), it was possible to identify the most stable structures. First, for the halide/H coadsorbate, the halide and the H atom are both separated by two vacant hollow sites. In addition, for the halide/pyridinium coadsorbate, the halide atom is in the hollow (for Br and I) or top (for Cl) position, while the pyridinium ion binds the surface through interaction with π-electrons of two C−C bonds and one C atom in a top, both distant by one vacant hollow site (Figure 11). Concerning the stepped model, we observed different configurations according to the metal nature. For the halide/H coadsorbate at Pd, the halide atom is linked to the edge side of the step with the H atom next to it, at the top layer of the step, in a hollow position. In the halide/pyridinium coadsorbate, the halide keeps the same position and the pyridinium ion binds the top layer close to the edge,

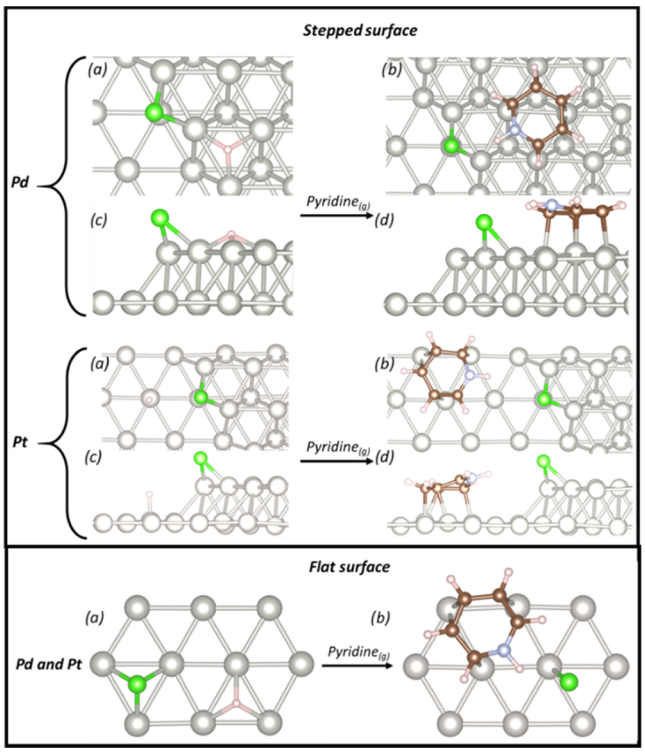

Figure 11. Most stable structures H/halide and pyridinium/halide coadsorbates at Pd and Pt. The top panel refers to the stepped model, while the bottom panel is related to the flat surface. In each frame, top views are represented in (a) and (b), while side views are displayed in (c) and (d). Colors: gray, metal; green, halide (here Cl); brown, C; pale blue, N; pale pink, H.

with one C−C bond in pi and the other C atoms in the top position. Regarding the Pt surface, the halide atom keeps the same configuration in the two coadsorbates in comparison with Pd. However, the H atom (in the top position) and the pyridinium (one C−C bond in pi, two C atoms in the top) ion are located at the bottom of the step close to the step edge. It needs to be mentioned that for the halide/H coadsorbate, the halide atom is shifted from the side of the edge to the edge top layer for I due to its large size in a hollow position.

We plotted reaction energies (ΔE) corresponding to pyridine protonation in Figure 12, for the stepped and the flat facets on the left and the right panels, respectively. First, comparing the clean surface to metal halides at the stepped model (see the left side in Figure 12), we observe that ΔE generally decreases for PdCl and PdBr vs pure Pd, whereas ΔE is significantly higher for PdI, shown in blue. This trend is less pronounced for Pt, where all of the ΔE are similar for every surface. This finding attests to acidic site formation by halide deposition at Pd, especially for Cl and Br, while the surface acidity is less impacted for Pt. Also, for the stepped model, Pt Brønsted acidity is always higher than for Pd. These results correspond to the catalytic results and characterization. Indeed, there is a significant decrease in acidity for the I-Pd catalyst in comparison with other halogenated Pd and comparable selectivity for all Pt halogenated catalysts. There is also a higher contribution of deoxygenated products over Pt catalysts in comparison with ether and acetal generation over Pd, indicating the higher strength of the acid sites over the Pt catalyst (Figure 2).

https://doi.org/10.1021/acscatal.3c00845
ACS Catal. 2023, 13, 6351−6364

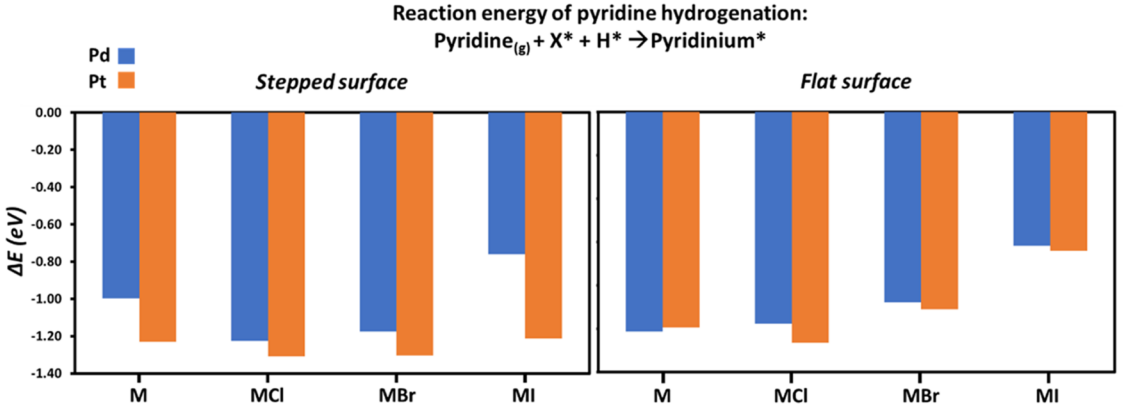

Figure 12. Reaction energies (ΔE) of the pyridine hydrogenation reaction for Pd (in blue) and Pt (in orange) surfaces, in the presence of Cl, Br, and I (MCl, MBr, and MI, respectively) and without any halide. Results are presented for the stepped and the flat model on the left and the right side, respectively. Low reaction energies attest to the high exothermicity of pyridine hydrogenation and thus the high Brønsted acidity of the surface. In the chart title, "*" denotes adsorbed species (in opposition to gas species) and X represents a halide element.

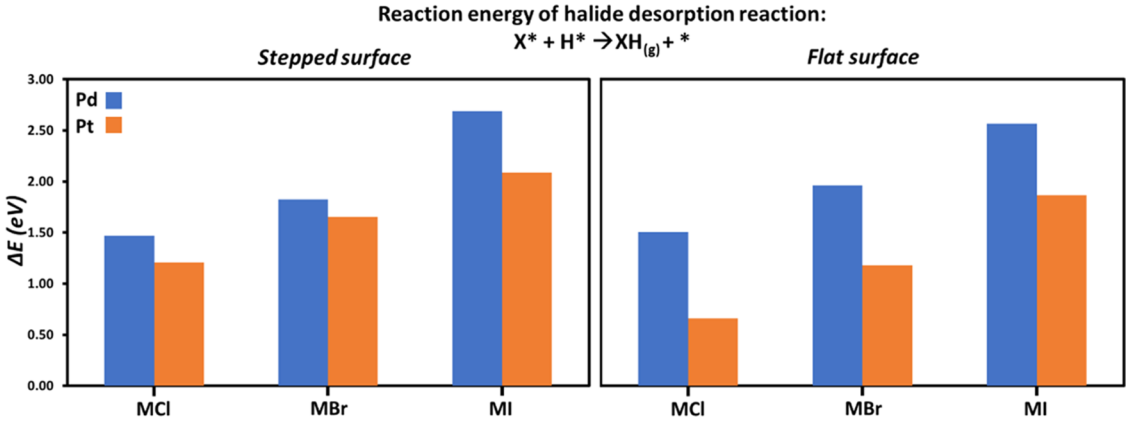

Figure 13. Reaction energy (ΔE) of the halide desorption reaction for Pd (in blue) and Pt (in orange) surfaces, in the presence of Cl, Br, and I (MCl, MBr, and MI, respectively) and without any halide. Results are presented for the stepped and the flat model on the left and the right side, respectively. High reaction energies attest to unfavorable halide desorption and thus high surface stability. In the chart title, "*" denotes adsorbed species (in opposition to gas species) and X represents a halide element.

However, such trends cannot be seen in the flat facet (Figure 12). Indeed, ΔE is always similar for Pt and Pd, either when the surface is clean or when bonded with halides. In addition, while ΔE is not impacted by Cl adsorption, it significantly increases for Br and I, making the pyridine protonation reaction less favorable. As a result, halide deposition at metals can modulate surface acidity. However, this effect is mostly observed in the presence of steps and defects, which are dominant when the nanoparticle size is considerably reduced. It explains the stronger effect of acid sites in the case of carbon-supported metal catalysts. FTIR results confirm the preferred deposition of halogens over steps and edges of Pt and Pd nanoparticles in comparison with the plane surface for Ru catalysts (Figure 7). It could be explained by the dissociation of PhHal over the steps and edges with modification of these sites by halogens or subsequent rearrangement of halogens on the surface.

The origin of this acidity is related to the charge of surface species, as suggested by the Bader charge analysis reported in Tables S5−S6, SI. Indeed, highly electronegative halides attract metal electrons, hence resulting in a localized partial positive charge at the catalyst surface. To compensate, the negative charge is shared between the halide element and the H atom. The more positive the metal charge, the more negative the adsorbed H charge. This situation with a partial negative charge at H is unfavorable, and the surface tends to release its proton more easily for Cl or Br, compared to I, hence explaining the Brønsted acidity difference between the three halide elements.

We also investigated surface stability. To that aim, we computed reaction energies (ΔE) related to halide desorption. Results are presented in Figure 13 for stepped and flat surfaces as previously. This reaction is never favorable since all of the ΔE are positive. However, notable differences can be observed between Pd and Pt metals. Indeed, ΔE is always higher for Pd in comparison with Pt, hence showing the high stability of Pd-based catalysts. In addition, we can see that for both metals ΔE increases continuously from Cl to I at the stepped and the flat model, hence explaining the difficulty in stabilizing Br and Cl, comparatively with I. The strong covalent bonding of metals with iodine improves stability; however, it results in a decrease of the activity of the catalysts. Finally, while Pd surface stability is not so much impacted by the step, it is clear when confronting the two panels in Figure 13 that regarding Pt, halides are much more stable in the presence of edges. That is why, in order to maximize the surface acidity and the probability of halide presence on the surface, it is preferable

https://doi.org/10.1021/acscatal.3c00845
ACS Catal. 2023, 13, 6351−6364

to design small-sized nanoparticle catalysts to increase the ratio of the defect, hence stabilizing surface halides.

4. CONCLUSIONS

We found that the halogen-modified metal catalysts enabled the in situ generation of acid sites by heterolytic dissociation of hydrogen directly over metal sites in the reaction. This is different from conventional bifunctional catalysts, where the active metal sites are associated with the metal nanoparticles and the acid sites are usually attributed to the oxide support. By high-throughput screening of various metals (Co, Ni, Ru, Pt, Pd, Rh) and halogens (Cl, Br, I) for furfural and HMF hydrogenation, we identified that halogenated Pd and Pt could generate the ether and products of deoxygenation by metal−acid bifunctional catalysis.

The characterization of the catalysts by FTIR, XPS, and TEM demonstrates the localization of halogens over edges and corners of Pd and Pt metal nanoparticles, resulting in heterolytic dissociation of hydrogen with the generation of acidity. The strength of acid sites increases according to the electronegativity of the elements in the order I < Br ≈ Cl. Interaction with iodine results in suppression of the catalytic activity of the elements due to the more covalent character of the bond. DFT modeling confirms the generation of acidity in the case of localization of the halogens at the defect sites of the nanoparticles.

■ ASSOCIATED CONTENT

Supporting Information

The Supporting Information is available free of charge at https://pubs.acs.org/doi/10.1021/acscatal.3c00845.

Metal and halogen content; GC-MS analysis of products; product selectivity and catalytic stability for HMF conversion; esterification between ethanol and acetic acid; metal particle size distribution; HAADF-STEM images and elemental mapping; XPS spectra; XAS linear combination and Br K-edge; and details of DFT simulations (PDF)

■ AUTHOR INFORMATION

Corresponding Authors

Andrei Khodakov − *UMR 8181—UCCS—Unité de Catalyse et Chimie du Solide, Univ. Lille, CNRS, Centrale Lille, ENSCL, Univ. Artois, F-59000 Lille, France;* orcid.org/0000-0003-4599-3969; Email: Andrei.Khodakov@univ-lille.fr

Jérémie Zaffran − *UMR 8181—UCCS—Unité de Catalyse et Chimie du Solide, Univ. Lille, CNRS, Centrale Lille, ENSCL, Univ. Artois, F-59000 Lille, France;* orcid.org/0000-0003-3176-6140; Email: Jeremie.Zaffran@univ-lille.fr

Vitaly Ordomsky − *UMR 8181—UCCS—Unité de Catalyse et Chimie du Solide, Univ. Lille, CNRS, Centrale Lille, ENSCL, Univ. Artois, F-59000 Lille, France;* orcid.org/0000-0002-4814-5052; Email: Vitaly.Ordomsky@univ-lille.fr

Authors

Yong Zhou − *UMR 8181—UCCS—Unité de Catalyse et Chimie du Solide, Univ. Lille, CNRS, Centrale Lille, ENSCL, Univ. Artois, F-59000 Lille, France*

Martine Trentesaux − *UMR 8181—UCCS—Unité de Catalyse et Chimie du Solide, Univ. Lille, CNRS, Centrale Lille, ENSCL, Univ. Artois, F-59000 Lille, France*

Maya Marinova − *University of Lille, CNRS, INRAE, Centrale Lille, University of Artois, F-59000 Lille, France*

Sergei Chernyak − *UMR 8181—UCCS—Unité de Catalyse et Chimie du Solide, Univ. Lille, CNRS, Centrale Lille, ENSCL, Univ. Artois, F-59000 Lille, France*

Jean-Charles Morin − *UMR 8181—UCCS—Unité de Catalyse et Chimie du Solide, Univ. Lille, CNRS, Centrale Lille, ENSCL, Univ. Artois, F-59000 Lille, France*

Melanie Dubois − *UMR 8181—UCCS—Unité de Catalyse et Chimie du Solide, Univ. Lille, CNRS, Centrale Lille, ENSCL, Univ. Artois, F-59000 Lille, France*

Samuel Eyley − *Sustainable Materials Lab, Department of Chemical Engineering, KU Leuven, Campus Kulak Kortrijk, 8500 Kortrijk, Belgium;* orcid.org/0000-0002-1929-8455

Wim Thielemans − *Sustainable Materials Lab, Department of Chemical Engineering, KU Leuven, Campus Kulak Kortrijk, 8500 Kortrijk, Belgium;* orcid.org/0000-0003-4451-1964

Vlad Martin-Diaconescu − *ALBA Synchrotron-CELLS, 08290 Cerdanyola del Vallès, Barcelona, Spain*

Complete contact information is available at: https://pubs.acs.org/10.1021/acscatal.3c00845

Notes

The authors declare no competing financial interest.

■ ACKNOWLEDGMENTS

XAS experiments were performed at the BL22-CLÆSS beamline at ALBA Synchrotron with the collaboration of ALBA staff as part of projects 2022035778 and 2022035785.

■ REFERENCES

(1) Wang, Y.; Tan, L.; Tan, M.; Zhang, P.; Fang, Y.; Yoneyama, Y.; Yang, G.; Tsubaki, N. Rationally Designing Bifunctional Catalysts as an Efficient Strategy To Boost CO2 Hydrogenation Producing Value-Added Aromatics. *ACS Catal.* **2019**, *9*, 895−901.

(2) Liu, X.; Wang, M.; Ren, X.; Guo, M.; Li, C.; Li, H.; Yang, Q. Activation of Carbonyl Groups via Weak Interactions in Pt/COF/SiO2 Catalyzed Selective Hydrogenation. *ACS Catal.* **2022**, *12*, 6618−6627.

(3) Li, X.; Chen, Y.; Liu, S.; Zhao, N.; Jiang, X.; Su, M.; Li, Z. Enhanced gasoline selectivity through Fischer-Tropsch synthesis on a bifunctional catalyst: Effects of active sites proximity and reaction temperature. *Chem. Eng. J.* **2021**, *416*, No. 129180.

(4) He, Y.; Itta, A. K.; Alwakwak, A.-a.; Huang, M.; Rezaei, F.; Rownaghi, A. A. Aminosilane-Grafted SiO2−ZrO2 Polymer Hollow Fibers as Bifunctional Microfluidic Reactor for Tandem Reaction of Glucose and Fructose to 5-Hydroxymethylfurfural. *ACS Sustainable Chem. Eng.* **2018**, *6*, 17211−17219.

(5) Wang, Z.; Yuan, X.; Cheng, Qa.; Zhang, T.; Luo, J. An efficient and recyclable acid−base bifunctional core−shell nano-catalyst for the one-pot deacetalization−Knoevenagel tandem reaction. *New J. Chem.* **2018**, *42*, 11610−11615.

(6) Kasipandi, S.; Bae, J. W. Recent Advances in Direct Synthesis of Value-Added Aromatic Chemicals from Syngas by Cascade Reactions over Bifunctional Catalysts. *Adv. Mater.* **2019**, *31*, No. e1803390.

(7) Metzger, K. E.; Moyer, M. M.; Trewyn, B. G. Tandem Catalytic Systems Integrating Biocatalysts and Inorganic Catalysts Using Functionalized Porous Materials. *ACS Catal.* **2021**, *11*, 110−122.

(8) van der Wal, L. I.; Oenema, J.; Smulders, L. C. J.; Samplonius, N. J.; Nandpersad, K. R.; Zecevic, J.; de Jong, K. P. Control and Impact

of Metal Loading Heterogeneities at the Nanoscale on the Performance of Pt/Zeolite Y Catalysts for Alkane Hydroconversion. *ACS Catal* **2021**, *11*, 3842−3855.
(9) Zecevic, J.; Vanbutsele, G.; de Jong, K. P.; Martens, J. A. Nanoscale intimacy in bifunctional catalysts for selective conversion of hydrocarbons. *Nature* **2015**, *528*, 245−248.
(10) Guisnet, M. "Ideal" bifunctional catalysis over Pt-acid zeolites. *Catal. Today* **2013**, *218−219*, 123−134.
(11) Cheng, K.; van der Wal, L. I.; Yoshida, H.; Oenema, J.; Harmel, J.; Zhang, Z.; Sunley, G.; Zecevic, J.; de Jong, K. P. Impact of the Spatial Organization of Bifunctional Metal-Zeolite Catalysts on the Hydroisomerization of Light Alkanes. *Angew. Chem., Int. Ed.* **2020**, *59*, 3592−3600.
(12) Wu, B.; Zheng, N. Surface and interface control of noble metal nanocrystals for catalytic and electrocatalytic applications. *Nano Today* **2013**, *8*, 168−197.
(13) Wu, D.; Han, D.; Zhou, W.; Streiff, S.; Khodakov, A. Y.; Ordomsky, V. V. Surface modification of metallic catalysts for the design of selective processes. *Catal. Rev.* **2022**, 1−47.
(14) Ntainjua N, E.; Piccinini, M.; Pritchard, J. C.; He, Q.; Edwards, J. K.; Carley, A. F.; Moulijn, J. A.; Kiely, C. J.; Hutchings, G. J. The Effect of Bromide Pretreatment on the Performance of Supported Au−Pd Catalysts for the Direct Synthesis of Hydrogen Peroxide. *ChemCatChem* **2009**, *1*, 479−484.
(15) Liu, P.; Qin, R.; Fu, G.; Zheng, N. Surface Coordination Chemistry of Metal Nanomaterials. *J. Am. Chem. Soc.* **2017**, *139*, 2122−2131.
(16) Liang, Q.; Li, Q.; Xie, L.; Zeng, H.; Zhou, S.; Huang, Y.; Yan, M.; Zhang, X.; Liu, T.; Zeng, J.; Liang, K.; Terasaki, O.; Zhao, D.; Jiang, L.; Kong, B. Superassembly of Surface-Enriched Ru Nanoclusters from Trapping-Bonding Strategy for Efficient Hydrogen Evolution. *ACS Nano* **2022**, *16*, 7993−8004.
(17) Wu, B.; Huang, H.; Yang, J.; Zheng, N.; Fu, G. Selective hydrogenation of alpha,beta-unsaturated aldehydes catalyzed by amine-capped platinum-cobalt nanocrystals. *Angew. Chem., Int. Ed.* **2012**, *51*, 3440−3443.
(18) Guo, M.; Li, H.; Ren, Y.; Ren, X.; Yang, Q.; Li, C. Improving Catalytic Hydrogenation Performance of Pd Nanoparticles by Electronic Modulation Using Phosphine Ligands. *ACS Catal.* **2018**, *8*, 6476−6485.
(19) F de L e Freitas, L.; Puértolas, B.; Zhang, J.; Wang, B.; Hoffman, A. S.; Bare, S. R.; Pérez-Ramírez, J.; Medlin, J. W.; Nikolla, E. Tunable Catalytic Performance of Palladium Nanoparticles for H2O2 Direct Synthesis via Surface-Bound Ligands. *ACS Catal.* **2020**, *10*, 5202−5207.
(20) Schoenbaum, C. A.; Schwartz, D. K.; Medlin, J. W. Controlling the surface environment of heterogeneous catalysts using self-assembled monolayers. *Acc. Chem. Res.* **2014**, *47*, 1438−1445.
(21) Wu, D.; Hernández, W. Y.; Zhang, S.; Vovk, E. I.; Zhou, X.; Yang, Y.; Khodakov, A. Y.; Ordomsky, V. V. In Situ Generation of Brønsted Acidity in the Pd-I Bifunctional Catalysts for Selective Reductive Etherification of Carbonyl Compounds under Mild Conditions. *ACS Catal.* **2019**, *9*, 2940−2948.
(22) Wu, D.; Zhang, S.; Hernández, W. Y.; Baaziz, W.; Ersen, O.; Marinova, M.; Khodakov, A. Y.; Ordomsky, V. V. Dual Metal−Acid Pd-Br Catalyst for Selective Hydrodeoxygenation of 5-Hydroxymethylfurfural (HMF) to 2,5-Dimethylfuran at Ambient Temperature. *ACS Catal.* **2021**, *11*, 19−30.
(23) Tong, Z.; Li, X.; Zhu, J.; Chen, S.; Dai, G.; Deng, Q.; Wang, J.; Yang, W.; Zeng, Z.; Zou, J.-J. Iodine-Modified Pd Catalysts Promote the Bifunctional Catalytic Synthesis of 2,5-Hexanedione from C6 Furan Aldehydes. *ChemSusChem* **2022**, *15*, No. e202102444.
(24) Zhu, C.; Hojo, H.; Einaga, H. Insights into the Hydrogenolysis Mechanism of Diphenyl Ether over Cl-Modified Pt/γ-Al2O3 Catalysts by Experimental and Theoretical Studies. *ACS Sustainable Chem. Eng.* **2022**, *10*, 8897−8907.
(25) Ravel, B.; Newville, M. ATHENA, ARTEMIS, HEPHAESTUS: data analysis for X-ray absorption spectroscopy using IFEFFIT. *J. Synchrotron Radiat.* **2005**, *12*, 537−541.
(26) Kresse, G.; Hafner, J. Ab initio molecular dynamics for liquid metals. *Phys. Rev. B* **1993**, *47*, 558−561.
(27) Hafner, J. Ab-initio simulations of materials using VASP: Density-functional theory and beyond. *J. Comput. Chem.* **2008**, *29*, 2044−2078.
(28) Perdew, J. P.; Burke, K.; Ernzerhof, M. Generalized Gradient Approximation Made Simple. *Phys. Rev. Lett.* **1996**, *77*, 3865−3868.
(29) Kresse, G.; Joubert, D. From ultrasoft pseudopotentials to the projector augmented-wave method. *Phys. Rev. B* **1999**, *59*, 1758−1775.
(30) Monkhorst, H. J.; Pack, J. D. Special points for Brillouin-zone integrations. *Phys. Rev. B* **1976**, *13*, 5188−5192.
(31) Wang, Y.; Zhao, D.; Rodríguez-Padrón, D.; Len, C. Recent Advances in Catalytic Hydrogenation of Furfural. *Catalysts* **2019**, *9*, 796.
(32) Manal, A. K.; Advani, J. H.; Srivastava, R. Bifunctional Acid-Base Zirconium Phosphonate for Catalytic Transfer Hydrogenation of Levulinic Acid and Cascade Transformation of Furfural to Biofuel Molecules. *ChemCatChem* **2022**, *14*, No. e202200576.
(33) Lan, X.; Pestman, R.; Hensen, E. J. M.; Weber, T. Furfural hydrodeoxygenation (HDO) over silica-supported metal phosphides − The influence of metal−phosphorus stoichiometry on catalytic properties. *J. Catal.* **2021**, *403*, 181−193.
(34) Hu, X.; Li, Z.; Wang, H.; Xin, H.; Li, S.; Wang, C.; Ma, L.; Liu, Q. Selective Hydrogenolysis of 5-Hydroxymethylfurfural to 2-Hexanol over Au/ZrO2 Catalysts. *ChemSusChem* **2022**, *15*, No. e202200092.
(35) Utaka, T.; Okanishi, T.; Takeguchi, T.; Kikuchi, R.; Eguchi, K. Water gas shift reaction of reformed fuel over supported Ru catalysts. *Appl. Catal., A* **2003**, *245*, 343−351.
(36) Mitra, J.; Zhou, X.; Rauchfuss, T. Pd/C-catalyzed reactions of HMF: decarbonylation, hydrogenation, and hydrogenolysis. *Green Chem.* **2015**, *17*, 307−313.
(37) Thananatthanachon, T.; Rauchfuss, T. B. Efficient Production of the Liquid Fuel 2,5-Dimethylfuran from Fructose Using Formic Acid as a Reagent. *Angew. Chem., Int. Ed.* **2010**, *49*, 6616−6618.
(38) Gawade, A. B.; Tiwari, M. S.; Yadav, G. D. Biobased Green Process: Selective Hydrogenation of 5-Hydroxymethylfurfural to 2,5-Dimethyl Furan under Mild Conditions Using Pd-Cs2.5H0.5PW12O40/K-10 Clay. *ACS Sustainable Chem. Eng.* **2016**, *4*, 4113−4123.
(39) Nishimura, S.; Ikeda, N.; Ebitani, K. Selective hydrogenation of biomass-derived 5-hydroxymethylfurfural (HMF) to 2,5-dimethylfuran (DMF) under atmospheric hydrogen pressure over carbon supported PdAu bimetallic catalyst. *Catal. Today* **2014**, *232*, 89−98.
(40) Ordomsky, V. V.; Luo, Y.; Gu, B.; Carvalho, A.; Chernavskii, P. A.; Cheng, K.; Khodakov, A. Y. Soldering of Iron Catalysts for Direct Synthesis of Light Olefins from Syngas under Mild Reaction Conditions. *ACS Catal.* **2017**, *7*, 6445−6452.
(41) Mihaylov, M.; Chakarova, K.; Hadjiivanov, K.; Marie, O.; Daturi, M. FTIR Spectroscopy Study of CO Adsorption on Pt−Na−Mordenite. *Langmuir* **2005**, *21*, 11821−11828.
(42) Bazin, P.; Saur, O.; Lavalley, J. C.; Daturi, M.; Blanchard, G. FT-IR study of CO adsorption on Pt/CeO2: characterisation and structural rearrangement of small Pt particles. *Phys. Chem. Chem. Phys.* **2005**, *7*, 187−194.
(43) Zeinalipour-Yazdi, C. D.; Willock, D. J.; Thomas, L.; Wilson, K.; Lee, A. F. CO adsorption over Pd nanoparticles: A general framework for IR simulations on nanoparticles. *Surf. Sci.* **2016**, *646*, 210−220.
(44) Chin, S. Y.; Williams, C. T.; Amiridis, M. D. FTIR Studies of CO Adsorption on Al2O3- and SiO2-Supported Ru Catalysts. *J. Phys. Chem. B* **2006**, *110*, 871−882.
(45) Wu, D.; Wang, Q.; Safonova, O. V.; Peron, D. V.; Zhou, W.; Yan, Z.; Marinova, M.; Khodakov, A. Y.; Ordomsky, V. V. Lignin Compounds to Monoaromatics: Selective Cleavage of C−O Bonds over a Brominated Ruthenium Catalyst. *Angew. Chem., Int. Ed.* **2021**, *60*, 12513−12523.
(46) Morgan, D. J. Resolving ruthenium: XPS studies of common ruthenium materials. *Surf. Interface Anal.* **2015**, *47*, 1072−1079.

https://doi.org/10.1021/acscatal.3c00845
ACS Catal. 2023, 13, 6351−6364

(47) Tur, V. A.; Okotrub, A. V.; Shubin, Y. V.; Senkovskiy, B. V.; Bulusheva, L. G. Chlorination of perforated graphite via interaction with thionylchloride. *Phys. Status Solidi B* **2014**, *251*, 2613−2619.
(48) Kang, E. T.; Ti, H. C.; Neoh, K. G. XPS Studies of Some Chemically Synthesized Polypyrrole−Organic Acceptor Complexes. *Polym. J.* **1988**, *20*, 845−850.
(49) Smith, D. K.; McCollum, J.; Pantoya, M. L. Effect of environment on iodine oxidation state and reactivity with aluminum. *Phys. Chem. Chem. Phys.* **2016**, *18*, 11243−11250.

https://doi.org/10.1021/acscatal.3c00845
ACS Catal. 2023, 13, 6351−6364